Supplementary Information

Low-Doping Clustering of Ti^{4+} in Monoclinic ZrO_2:

Photoluminescence and Formation Mechanism

Guo-Hui Pan[1,2]*, Xuesong Qu[3], Xiaobao Ma[1], Ligong Zhang[1], Liangliang Zhang[1], Huajun Wu[1], Hao Wu[1], Zhiming Shi[1]*, Jiahua Zhang[1]*

[1]*State Key Laboratory of Luminescence Science and Technology, Changchun Institute of Optics, Fine Mechanics and Physics, Chinese Academy of Sciences, 3888 Dong Nanhu Road, Changchun 130033, China.*
[2]*State Key Laboratory of Advanced Manufacturing for Optical System, Changchun Institute of Optics, Fine Mechanics and Physics, Chinese Academy of Sciences, 3888 Dong Nanhu Road, Changchun 130033, China.*
[3]*College of Science Education*, C*hangchun Normal University, Changchun 130032, China.*

To whom correspondence should be addressed: pangh@ciomp.ac.cn, shizm@ciomp.ac.cn, zhangjh@ciomp.ac.cn

Materials and Methods

A. Chemicals and materials preparation

All chemicals used in this study were of analytical grade and were used without further purification. Weighed amounts of the high purity of starting materials (ZrO_2 (99.99%, metals basis, without Hf or HfO_2) and TiO_2 (99.0%, metals basis), Aladdin Industrial Inc., China) were homogenized by grinding, calcined at 1300 °C (4 h, air). The singly doped samples are m-ZrO_2:$x$$Ti^{4+}$ (x= 0.02%, 0.05%, 0.1%, 0.2%, 0.5%, 1%, 2%, 3%, 4% and 8%). All concentrations are nominal and in the units of mol.

B. Characterization and measurements

The room-temperature steady state photoluminescence emission and excitation spectra were acquired on a F7000 spectrometer (Hitachi, Japan) equipped with a 150 W Xenon lamp as excitation source. The spectra were corrected to the instrument responses. The temperature-dependent PL emission measurements (13–300 K) employed a QEPro fiber optic spectrometer (Ocean Optics, USA), where the powdered samples mounted in a closed-cycle helium cryostat were photoexcited by an FLS 920 spectrofluorometer (Edinburgh Instruments, UK) equipped with a 450 W xenon lamp. A 360 nm cut-off filter was routinely used. Decay dynamics utilized an optical parametric oscillator (OPO) pulsed excitation source, with signals analyzed via a Triax550 spectrometer (Horiba, France) and a TDS3052 digital oscilloscope (Tektronix, USA).

X-ray absorption spectroscopy (XAS) experiments were conducted at the Ti K-edge (4966 eV) on beamline BL20U1 at Shanghai synchrotron radiation facility (SSFF). A Si [111] double crystal monochromator detuned by 50% minimized the harmonics. Energy resolution was $\Delta E/E \sim 2.0\times10^{-4}$ at 5 keV. Data of all samples were acquired in fluorescence mode using silicon drift detector (Vortex, Hitachi, USA). All measurements occurred at ambient conditions. Ti foils served as energy calibration for Ti K-edge. XAS data were reduced using the Demeter software package.[1] A linear function was subtracted from the pre-edge region, followed by edge-jump normalization using Athena. The R_{bkg} cut-off value was set to 1.0 to eliminate the artificial peaks below 1.0 Å. The EXAFS data were derived by subtracting a third-order polynomial atomic background to isolate $\chi(k)$ in k-space, then averaged over three scans to enhance the signal-to-noise ratios. The $\chi(k)$ data were weighted by k^2 (Ti K-edge), then fast Fourier transformed (FFT) to r-space using a Haining window

function (Δk = 1). EXAFS *r*-space fitting via Artemis software extracted microstructural parameters. Using the known structure for *m*-ZrO_2.

C. Computational methodology

For point defect/cluster systems, we performed DFT calculations using the projector augmented-wave (PAW) method in the Vienna Ab Initio Simulation Package (VASP) to examine the charge density around oxygen vacancy (Isosurface of the square of the vacancy wave function),[2-4] and compute the defect formation energies (DFEs). Full geometry relaxation of the ZrO_2 primitive unit cell (20 atoms) was first performed considering a 5 × 5 × 5 Monkhorst−Pack k-mesh (25 irreducible *k*-points),[5] with atomic forces and total energy minimized to threshold of 0.02 eV/Å and 10^{-4} eV, respectively. Defect-containing supercells were constructed from a 3 × 3 × 3 expansion of the relaxed unit cell. Subsequent relaxations used a Γ-centered 2 × 2 × 2 *k*-mesh, consistent with the mesh for accurate energy calculations. In all the self-consistent field (SCF) calculations, the cutoff energy of the plane-wave basis was set to 500 eV, with the valence-electron configurations: Zr $4d^25s^2$, Ti $3d^24s^2$, and $O2s^22p^4$. The 2 × 2× 2 *k*-points grids were used for sampling in the Brillouin zone.

DFEs of different defect configuration were estimated using the supercell approach, and may thus be computed with the following formula[6]:

$$\Delta_f H^{D,q}\left(\mu_{E_F}\right) = E_{DFT}^{D,q} - E_{DFT}^{host} + \sum_i n_i\mu_i + q\left(\mu_{E_F} + E_{VBM}^{host}\right) + \Delta_{corr} \quad (2)$$

where $\Delta_f H^{D,q}$ is the DFE of a defect *D* in a charge state *q*, $E_{DFT}^{D,q}$ is the DFT total energy of the faulted structure, E_{DFT}^{host} is the DFT totalenergy of the host structure, n_i is the number of atoms of the *i*th species added ($n_i < 0$) or removed ($n_i > 0$) from the ideal material, μ_i is the chemical potential of the related species, μ_{E_F} is the Fermi level, E_{VBM}^{host} corresponds to the valence band maximum (VBM) of the host material, and Δ_{corr} is associated with various corrections of spurious effects. In the present supercell calculations, defect formation energies for neutral defects are evaluated using charge-neutral supercells, as is standard practice. Since the system remains globally neutral (net charge q=0), the finite-size correction term Δ_{corr}—normally introduced to mitigate spurious electrostatic interactions between a charged defect and its periodic images—is omitted. This omission is justified because, in the case of neutral defects within a neutral supercell, long-range Coulomb interactions that cause

significant finite-size errors for charged defects become negligible. The approach is well established in the computational literature.[6,7] Consequently, our results and conclusions, which rely on comparisons among different neutral defect configurations, are unaffected by this class of supercell correction.

Table S1 Curvefit parameters for the Ti-*K* edge EXAFS of m-ZrO_2:*x*Ti^{4+} (S_0^2=0.80）.

Sample	Path	C.N.	R (Å)	σ^2(Å^2)	ΔE (eV)	R factor
ZrO_2:0.5%Ti^{4+}	Ti-O1	1.8±0.2	1.89±0.02	0.0003*	-4.1±2.6	0.0084
	Ti-O2	1.0±0.2	2.06±0.03	0.0003*		
	Ti-Zr1	6.1±1.5	3.51±0.03	0.0160*		
	Ti-Zr2	2.5*	3.84±0.02	0.0004±0.0013		
	Ti-Zr3	1.8*	4.02±0.03	0.0004±0.0013		
	Ti-Ti1	0.8±0.6	3.24±0.06	0.0150*		
ZrO_2:2%Ti^{4+}	Ti-O1	2.0±0.2	1.92±0.02	0.0004*	-0.5±2.6	0.0097
	Ti-O2	1.1±0.3	2.13±0.03	0.0004*		
	Ti-Zr1	5.9±1.3	3.53±0.03	0.0135*		
	Ti-Zr2	2.2*	3.86±0.02	0.0006±0.0024		
	Ti-Zr3	1.8*	4.05±0.05	0.0006±0.0024		
	Ti-Ti1	1.2±0.7	3.27±0.05	0.0155*		
ZrO_2:8%Ti^{4+}	Ti-O1	1.8±0.2	1.90±0.02	0.0004*	-0.4±1.8	0.0052
	Ti-O2	1.4±0.2	2.08±0.03	0.0004*		
	Ti-Zr1	5.5±1.1	3.49±0.02	0.0155*		
	Ti-Zr2	2.2*	3.86±0.03	0.0055±0.0034		
	Ti-Zr3	1.8*	4.06±0.04	0.0055±0.0034		
	Ti-Ti1	1.5±0.7	3.25±0.04	0.0200*		

C.N.: coordination numbers; *R*: bond distance; σ^2: Debye-Waller factors; ΔE: the inner potential correction. *R* factor: goodness of fit. *fitting with fixed parameter.

The applied constrains during the *Ti*-K edge EXAFS fitting

The weak Ti-*K* edge absorption and low Ti^{4+} doping concentration in our samples yielded EXAFS data with reduced signal-to-noise ratio at room temperature. This results in noisier averaged spectra (Fig. 4a) and restricts the Fourier transforms ranges. The *k*-space EXAFS data for our samples are reliable only to ~10.3 Å^{-1}, limiting the number of fittable parameters.

Ti-*K* edge EXAFS fits were performed in the *r*-space by summing the theoretical FEFF path contributions using ARTEMIS.[1] The FFT range was 2.5–10.3 Å^{-1} and the *r*-space fit range was 1.0–4.0 Å, yielding 16.7 independent data points by Stern's

criteria.[8] Due to *m*-ZrO_2's lower symmetry, the second neighbor peak requires accounting for three distinct subshells during EXAFS analysis, necessitating additional fitting parameters. Within the r-space range of 1.0–4.0 Å—established from Zr-*K* edge data—this region typically contains one shell of 7 oxygen first neighbors and two subshells of Zr second neighbors (7 and 4 atoms, respectively). In a series of test fits, we found that split-peak fitting of the Ti–O peak and second Ti–Zr subshell due to ion relaxation were required for overall good results. Final fits incorporated two Ti–O pairs, three Ti–Zr pairs, and one Ti–Ti pair. Each pair included three parameters: coordination number (N), half-path length adjustment (Δr), and the mean-square relative displacement (σ^2, i.e., the disorder level). Two global parameters were added: amplitude reduction factor S_0^2 and edge-energy shift ΔE_0 (energy offset between experimental data and theoretical k=0 reference). Herein, however, there are not enough degrees of freedom to allow all these parameters to vary independently, based on Stern's criteria above.[8] Consequently, to ensure robust fits to FT magnitude/imaginary components and reasonable parameter values, we constrained parameters as follows: σ^2 values for Ti–O pairs, first Ti–Zr pair, and Ti–Ti pair were fixed, while neighbor numbers for distant Ti–Zr pairs were set to ~4 (reflecting negligible Ti substitution in the second subshell due to low fit amplitude). Higher disorder parameters for Ti–Zr/Ti–Ti pairs were fixed to account for cation relaxation from undersized Ti_{Zr} substitution and the presence of nearby oxygen vacancies. The summed coordination numbers of the first Ti–Zr and Ti–Ti subshells were deliberately adjusted to approach 7—matching the second Zr–Zr subshell coordination in *m*-ZrO_2. S_0^2 was fixed at 0.8, consistent with Ti-*K* edge EXAFS standards for TiO_2.[9-11] These constraints reduced varied parameters to 12—below the 16.7 independent points limit—while ensuring robust fits to FT magnitude/imaginary components.

Some Ti atoms may also be present in the second and third subshells of Ti absorbers, indicating that the actual number of Ti neighbor atoms likely exceeds the values listed in Table S1. Consequently, significantly larger Ti^{4+} clusters are expected to form in the *m*-ZrO_2 lattice.

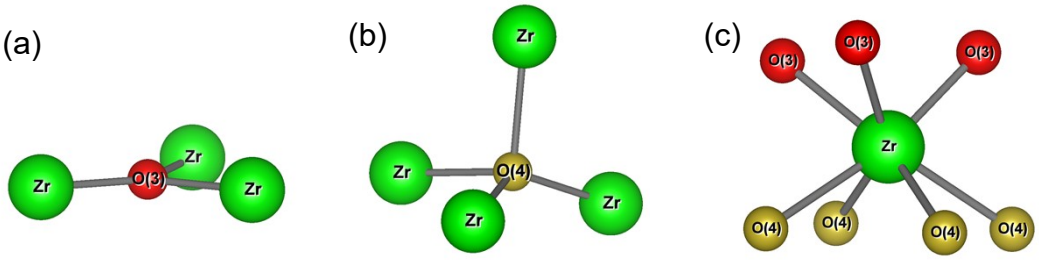

Fig. S1 Coordination environments in *m*-ZrO_2: O(3) atoms reside in trigonal planes (a), O(4) atoms occupy tetragonal sites (b), and Zr atoms exhibit 7-coordination (c). Green spheres represent Zr atoms; red and orange spheres denote O(3) and O(4) atoms, respectively. The depicted coordination geometries are consistent with the standard structural model of *m*-ZrO_2 (see, e.g., Ref. 12; and are also described/employed in related computational studies such as Ref. 13).

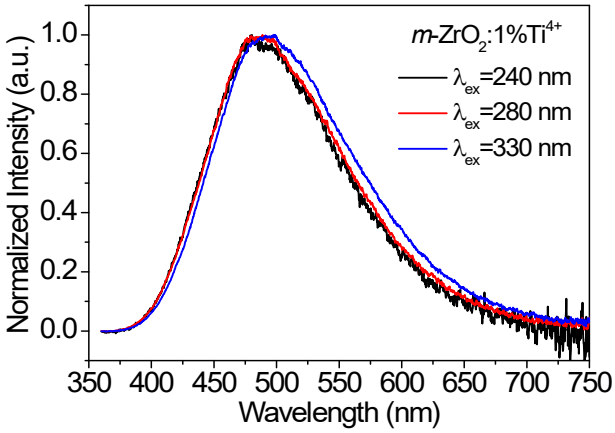

Fig. S2 Normalized PL emission spectra of *m*-ZrO_2:1%Ti^{4+} sample under different excitation wavelengths at room temperature. A slight spectral shift occurred under longer wavelength excitation at 330 nm, which arises primarily from spectral overlap with either the residual trace emissions of clustered Ti^{4+} ions or the emissions of isolated Ti^{4+} ions residing in nonequivalent crystal-field sites.

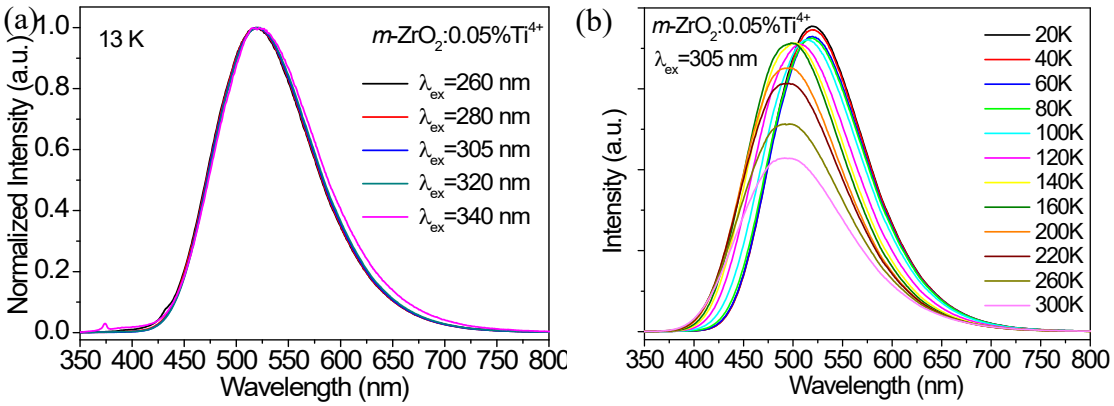

Fig. S3 (a) Normalized PL emission spectra of *m*-ZrO_2:0.05%Ti^{4+} sample under different excitation wavelengths at 13 K. Due to the lower Ti^{4+} concentration, the *m*-ZrO_2:0.05%Ti^{4+} sample exhibits predominantly isolated Ti^{4+} ion distribution, with negligible clustering significance; (b) Temperature-dependent PL emission spectra of *m*-ZrO_2:1%Ti^{4+} (λ_{ex}=305 nm).

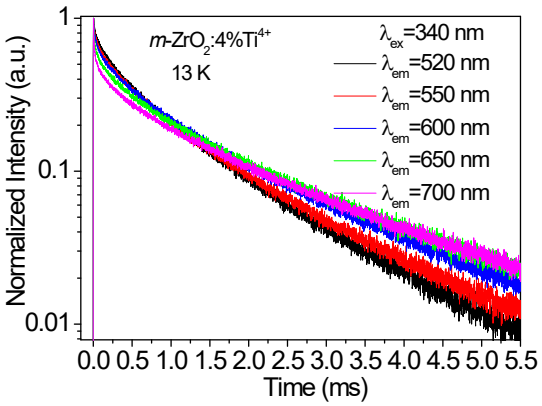

Fig. S4 Fluorescence decay traces of *m*-ZrO_2:4%Ti^{4+} at 13 K under 340 nm excitation, measured at selected emission wavelengths.

References

1 B. Ravel and M. Newville, ATHENA, ARTEMIS, HEPHAESTUS: data analysis for X-ray absorption spectroscopy using IFEFFIT, *J. Synchrotron Radiat.*, 2005, **12**, 537–541.

2 G. Kresse and J. Furthmüller, Efficiency of ab-initio total energy calculations for metals and semiconductors using a plane-wave basis set, *Comput. Mater. Sci.*, 1996, **6**, 15–50.

3 G. Kresse and J. Furthmüller, Efficient iterative schemes for ab initio total-energy calculations using a plane-wave basis set, *Phys. Rev. B*, 1996, **54**, 11169–11186.

4 G. Kresse and D. Joubert, From ultrasoft pseudopotentials to the projector augmented-wave method, *Phys. Rev. B*, 1999, **59**, 1758–1775.

5 H. J. Monkhorst and J. D. Pack, Special points for Brillouin-zone integrations, *Phys. Rev. B*, 1976, **13**, 5188–5192.

6 A. Goyal, P. Gorai, H. Peng, S. Lany and V. Stevanović, A computational framework for automation of point defect calculations, *Comput. Mater. Sci.*, 2017, **130**, 1–9.

7 C. Freysoldt, B. Grabowski, T. Hickel, J. Neugebauer, G. Kresse, A. Janotti, C. G. Van de Walle, First-principles calculations for point defects in solids, *Rev. Mod. Phys.,* 2014, **86**, 253–305.

8 E. A. Stern, Number of relevant independent points in X-ray-absorption fine-structure spectra, *Phys. Rev. B* 1993, **48**, 9825–9827.

9 R. Bassiri, M. R. Abernathy, F. Liou, A. Mehta, E. K. Gustafson, M. J. Hart, H. N. Isa, N. Kim, A. C. Lin, I. MacLaren, I. W. Martin, R. K. Route, S. Rowan, B. Shyam, J. F. Stebbins, and M. M. Fejer, Ordering, disorder and mixing: The atomic structure of amorphous mixtures of titania and tantala, *J. Non-Cryst. Solids* 2016, **438**, 59–66.

10 L. Pan, M. Ai, C. Huang, L. Yin, X. Liu, R. Zhang, S. Wang, Z. Jiang, X. Zhang, J.-J. Zou, and W. Mi, Manipulating spin polarization of titanium dioxide for efficient photocatalysis, *Nat. Commun.* 2020, **11**, 418.

11 Y. Zong, K. Fujita, H. Akamatsu, S. Nakashima, S. Murai, and K. Tanaka, Local structure of amorphous EuO–TiO_2 thin films probed by X-Ray absorption fine structure, *J. Am. Ceram. Soc.* 2012, **95**, 716–720.

12 M. Winterer, R. Delaplane, R. McGreevy, X-ray diffraction, neutron scattering and EXAFS spectroscopy of monoclinic zirconia: analysis by Rietveld refinement and reverse Monte Carlo simulations, *J. Appl. Cryst.*, 2002, **35**, 434-442.

13 W. Lafargue-Dit-Hauret, R. Schira, C. Latouche and S. Jobic, Theoretical calculations meet experiment to explain the luminescence properties and the presence of defects in m-ZrO_2, *Chem. Mater.*, 2021, **33**, 2984–2992.